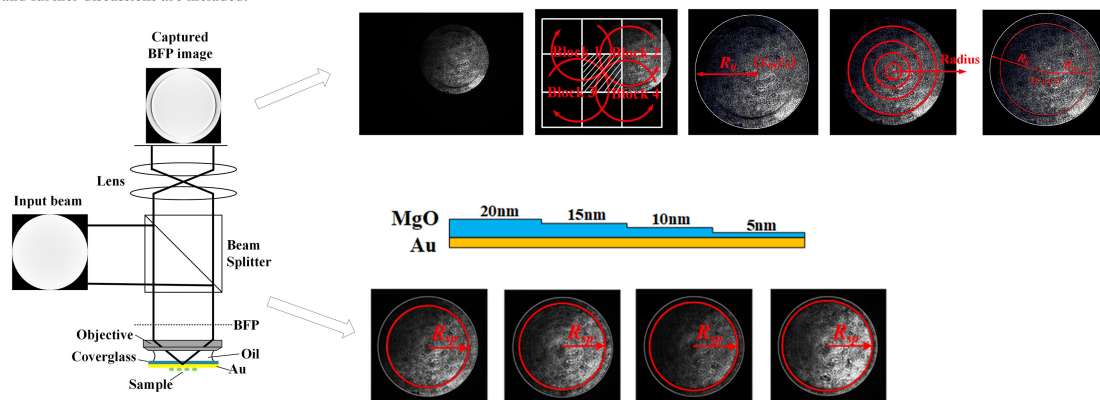


# Identification of Plasmonic Absorption Profile in Surface Plasmon Microscopy Using Morphology

Volume 10, Number 6, December 2018

Bei Zhang  
 Chengqian Zhang  
 Qiusheng Wang  
 Peng Yan  
 Jing Wang

Surface Plasmon microscopy (SPM) provides the capability of measuring surface properties of sub-nanometer layers within the diffraction limited order. In a typical SPM, small changes correspond to surface plasmons (SPs) absorption profile variations on a reflecting back focal plane (BFP), which can be monitored in real-time. However, the lack of fast and high-accurate identification method on SPs profiles has posed significant challenges on objective-coupled SPM instruments, and also limited their practical applications in fast phenomenon sensing and image batch processing. Here we propose a morphological method to identify the SPs absorption profiles. It can extract the SPs profile information from experimentally recorded BFP images with low quality properly and automatically. Experimental verification and further discussions are included.



# Identification of Plasmonic Absorption Profile in Surface Plasmon Microscopy Using Morphology

Bei Zhang<sup>1</sup>,<sup>1</sup> Chengqian Zhang<sup>1</sup>,<sup>1</sup> Qiusheng Wang,<sup>1</sup> Peng Yan,<sup>1</sup>  
and Jing Wang<sup>2</sup>

<sup>1</sup>Department of Automation Science and Electrical Engineering, Beihang University, Beijing 100191, China

<sup>2</sup>Department of Electrical and Electronic Engineering, University of Nottingham Ningbo, Ningbo 315100, China

DOI:10.1109/JPHOT.2018.2875019

1943-0655 © 2018 IEEE. Translations and content mining are permitted for academic research only. Personal use is also permitted, but republication/redistribution requires IEEE permission. See [http://www.ieee.org/publications\\_standards/publications/rights/index.html](http://www.ieee.org/publications_standards/publications/rights/index.html) for more information.

Manuscript received September 20, 2018; accepted October 5, 2018. Date of publication October 9, 2018; date of current version October 29, 2018. This work was supported by the National Natural Science Foundation of China under Grant 61405006; and in part by the open funding project of the State Key Laboratory of Virtual Reality Technology and Systems under Grant BUAA-VR-15KF-04. Corresponding author: B. Zhang (e-mail: bei.zhang@buaa.edu.cn).

**Abstract:** Surface plasmon microscopy (SPM) provides the capability of measuring surface properties of subnanometer layers within the diffraction limited order. In a typical SPM, small changes correspond to surface plasmons (SPs) absorption profile variations on a reflecting back focal plane (BFP), which can be monitored in real-time. However, the lack of fast and high-accurate identification method on SPs profiles has posed significant challenges on objective-coupled SPM instruments, and also limited their practical applications in fast phenomenon sensing and image batch processing. Here we propose a morphological method to identify the SPs absorption profiles. It can extract the SPs profile information from experimentally recorded BFP images with low quality properly and automatically. Experimental verification and further discussions are included.

**Index Terms:** Surface plasmon microscopy, image processing, morphology, identification.

## 1. Introduction

Surface plasmons (SPs) are electromagnetic waves propagating along the interface between a metal and a dielectric layer. Propagation properties of SPs are extremely sensitive to small changes on the interface, which makes it widely applied in biological and chemical sensing [1]. A typical coupling method to excite SPs is the so-called Kretschmann configuration which utilizes a prism with high index as coupling agent and is characterized by a dark band on the reflected light beam [2]. This configuration has achieved great success in both academia and industries, but suffers from poor spatial resolution, which is worse than the diffraction limitation of conventional optical microscopy [2]. During the last twenty years, there has been a great interest in combining excellent sensitivity of SPs with high spatial resolution, which provides a route to microscopic sensing or label-free biological imaging. Kano proposed a scanning surface plasmon microscopy (SPM) that used immersion objective lens to excite SPs within the focal spot confined region [3]. In this configuration, plasmonic properties of detected materials are translated by variations of SPs absorption profiles on back focal plane (BFP) of objective lens and exhibits as symmetrical absorption crescents or dark

absorption rings [3], [4] when using linearly-polarized or radially-polarized illumination respectively. It is obvious that fast and high-accurate identification of plasmonic absorption profile on the BFP determines the detection accuracy of smaller changes on the interface. Meanwhile, fast and high-accurate identification of SPs profile on batches of BFP images is of extremely importance for practical applications of the technique in fast phenomenon tracing and imaging reconstruction.

Besides the intensity scanning SPM, the identification of SPs profiles is also highly required in wide-field SPM [5]–[9]. Its basic principle is to output collimated light at a specified incident angle onto the sample and collect the reflected wide-field image. Two configurations have been proposed to implement wide-field SPM. One is to use a spatial light modulator (SLM) [5]–[7] and the other one is to use a mechanical stage [8], [9]. Here we specifically discuss the former configuration since the latter one does not give a BFP image with SPs absorption profiles [8], [9]. In the SLM based wide-field SPM configuration, the illumination incident angle is controlled by shifting radius of the illumination ring in BFP. One issue associated with wide-field SPM is that its image contrast is significantly influenced by incident angle of the illumination. Conventional method is to use a preset sample for instance a uniform gold surface, take a series of images and fit its corresponding surface reflectivity curve. Then the incident angle for the illumination is defined as the minimum or a specified angle with the steepest reflectivity slope. Theoretically, the wide-field image can be obtained by fixing the incidence at the defined specified angle. However, in practice, a spatial light modulator [5]–[7] or translation stage [8], [9] is utilized to tune the incident angle around the defined angle and search for wide-field images with better contrast. That is because the fitted surface reflectivity curve is obtained using the pre-set uniform sample not the tested sample while the SPs excitation angles vary with the tested materials. For this reason, it is suggested to rapidly identify the corresponding plasmonic excitation angle of the specific sample and then define the correspondingly required illumination angle. Besides, the identification in wide-field SPM can determine not only the excitation angle but also the p-polarized direction, which allows blocking the s-polarized illumination in linearly-polarized system and enhancing the contrast in the wide-field images.

Another potential application of the identification is our recently proposed common-path interferometric SPM with pupil function engineering [10], [11]. Its basic configuration is similar as the intensity scanning SPM proposed by Kano [3] except that a virtual pinhole is defined on the focal spot. When the sample is at defocus, the virtual pinhole makes only the normal incidence ('reference') and the beam portion that excites SPs ('Signal') can pass and interfere on imaging plane. Periodic ripples caused by the interference give the phase information of SPs, which corresponds to the sample characteristics. To enhance the periodic ripples, we apply a SLM to modulate the pupil plane and make only the beam portions that contribute to the interference can pass and interfere. Since the beam portion for SPs excitation is determined by the tested sample, rapid and high-accurate location of the SPs excitation angle can be applied to dynamically control the illumination for the specific sample.

Theoretically, SPs can be identified by searching for the minimum on reflecting BFP images. However, in practice, SPs absorption dips are covered by coherent noise on experimentally recorded BFP images when using laser as the illumination source. It imposes great challenges on the identification and limits automatic operation of SPM instruments. To acquire a clear BFP image, a common strategy in SPM is to use a diffuser to weaken the spatial coherence of laser source and decrease the coherent noise on BFP images. However, this method is at the cost of spatial resolution and is only applicable for uniform sample in a scanning SPM. One direct and conventional method is to capture the 1-D intensity data along the p-polarized direction and identify the minimum as the SPs excitation angle. It suffers from several disadvantages: 1) In the linearly-polarized case, it is required to define the exact direction of p-polarization, which is generally determined by the technician; 2) the objective-coupled SPM excites SPs in 2-dimensions while the statistics is carried out along the 1-D line scan, which gives relatively inaccurate results; 3) since its basic principle is to find the minimum value and define it as the SPs excitation angle, the identification is vulnerable to random coherent noises in BFP images. More recently, an optimized 1-D identified method has been proposed [12], which is to capture the 1-D line-scan intensity data along the s-polarized direction and p-polarized directions respectively and obtain a relatively accurate plasmonic angular

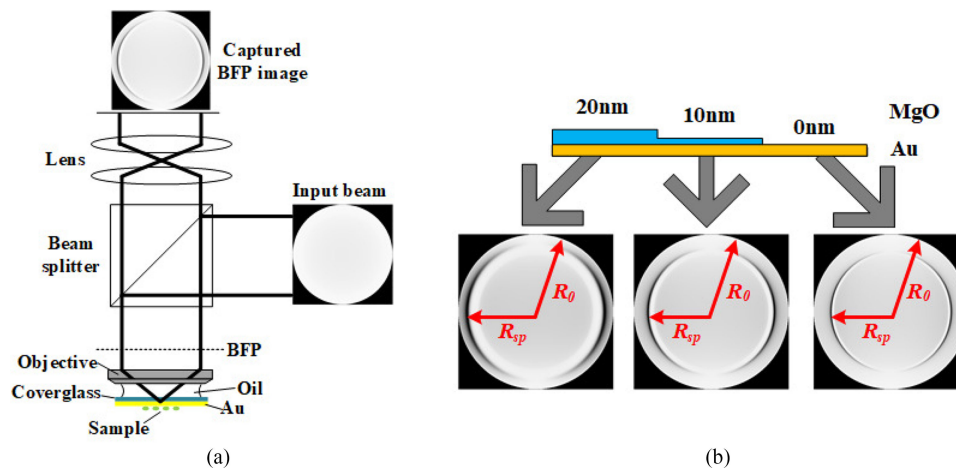


Fig. 1. (a) Configuration of objective-coupled intensity scanning SPM; (b) Calculated 2-D BFP images when using bare gold, 10 nm and 20 nm MgO coated samples;  $R_0$  and  $R_{sp}$  are radii of clear aperture and SPs absorption profile respectively.

response by dividing the two sets of intensity data. This optimized method gives higher accurate result but still uses the 1-D intensity data and is vulnerable to random noises. Since SPs absorption profiles exhibit as two-dimensional distribution on BFP, it is recommendable to identify the SPs profile in two-dimensions as it can average the effect of random noises and give a smaller standard deviation than the 1-D identification method. For this reason, 2-D identification approach is capable of handling low-quality BFP images with relatively severe coherent noises. Previous works [3] and [4] fitted SPs absorption profiles with a circle but did not illustrate the identification method. And so far, there has been no proper 2-D identification approach in the fields. This work aims to present an effective 2-D identification approach which can be implemented in SPMs to automatically fit the SPs profile and solve the essential problem in instrumentation of SPMs. To the best of the authors' knowledge, it is the first time to specifically illustrate a 2-D identification method in objective-coupled SPM.

## 2. Plasmonic Absorption Profile in SPM

We take the objective-coupled scanning SPM (Fig. 1(a)) as the example to illustrate the identification principle. Readers are referred to [3], [4] for the details of SPs excitation using immersion objectives. A He-Ne laser with a wavelength of 632.8 nm is utilized as the light source. The tested sample is positioned on the gold-coated cover glass. All the test is carried out in air condition. The collimated illumination is focused on the sensor-chip and generates a confined focal spot region for the SPs excitation. Within the optical cone near the sample, only a specific angle can fulfill the SPs excitation conditions, which is reflected back to the system and features on absorption dips on the BFP of objective lens. A detector is placed on the conjugate plane to capture the BFP images. The optimal plasmonic excitation angle, corresponding to the radius of absorption profiles on BFP, is extremely sensitive to small changes on the interface. Fig. 1(b) gives the calculated plasmonic distributions on the BFP when using linearly polarized illumination and MgO layers with different thickness. The parameters of refractive index and thickness in the calculation and experiment are shown in Table 1.

As shown in Fig. 1(b), SPs profiles distribute as symmetrical absorption crescents, which are caused by two separate effects: the asymmetry of intensity along a circle (due to the varying s/p polarized ratio) and the radii of the circle (due to the varying thickness of MgO). The radii of the SPs absorption crescents are related with the thickness of the MgO layers by Fresnel multilayer reflection theory [6]. More details on the Fresnel multilayer reflection theory can be found in Appendix B of

TABLE 1  
Parameters in the Simulation and Experiment

Material	Refractive index@632.8nm	Thickness/nm
Coupling oil	1.518	$\infty$
Glass/BK7	1.518	170
Au	0.184+3.431i	46
Air	1.000	$\infty$
MgO	1.735	0-20

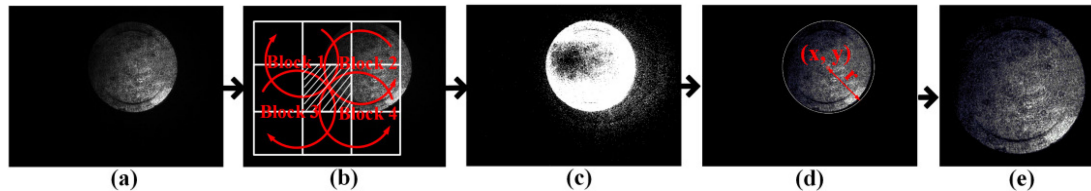


Fig. 2. (a) Experimentally measured BFP image using the bare sensor-chip with an immersion objective lens with a NA of 1.35; (b) Schematic of the local threshold value; (c) The binary image processed with a combination of global and local threshold; (d) Location of the CA. (e) Cropped image.

Tan's thesis [6]. According to Abbe's sine condition, we get:

$$\begin{cases} NA = n_0 \sin \theta_{\max} \\ \sin \theta_{\max} / \sin \theta_{\text{sp}} = R_0 / R_{\text{sp}} \end{cases} \quad (1)$$

in which  $R_{\text{sp}}$  indicates the radius of the aperture and  $R_0$  is the radius of SPs profile as shown in Fig. 1(b). The term  $n_0$  denotes the refractive index of coupling oil.  $\theta_{\max}$  is the maximum incident angle which is determined by the numerical aperture (NA) of an objective lens.  $\theta_{\text{sp}}$  is the SPs excitation angle which is less than  $\theta_{\max}$  to make sure SPs can be excited. The SPs optimal excitation angle can be obtained by identifying the location of the plasmonic absorption profile on BFP and calculating the radius of the absorption crescents.

### 3. Identification Procedures

In this section we describe how to identify the SPs absorption profiles on experimentally acquired BFP images. We select BFP images with extraordinary uneven brightness and poor quality to show efficiency and good performance of the proposed method. Fig. 2(a) shows an experimental image of the BFP captured by CCD ( $1292 \times 964$  with pixel size of  $3.75 \mu\text{m}$ ). In the experimental system, we employ a 1.35 NA oil-immersion lens and a He-Ne laser with a wavelength of 632.8 nm. The sample that we utilize is 46 nm Au coated with 5 nm MgO by magnetron sputtering. In our experiment, the thicknesses of the sputtered MgO layers are initially controlled by crystal oscillators in the magnetron sputter, which gives a precision with an error below 0.1 nm. After that, in order to obtain an independent measure of the thicknesses of the layers, they are measured from the top surface using a spectroscopic ellipsometer (alpha-SE J. A. Woollam (Inc.), Lincoln, Nebraska, USA). The light disk in the image corresponds to the aperture of the objective, and two dark arcs correspond to the SPs absorption profile. We classify the identification procedures into three steps: firstly to locate and crop the region of interest (ROI) (Section 3.1), secondly to identify the optical axis center (Section 3.2) and finally to identify the SPs absorption profile (Section 3.3). Hough Transform, morphological method and least-square method are combined for automatic and high precision identification of SPs absorption profile on BFP image respectively.

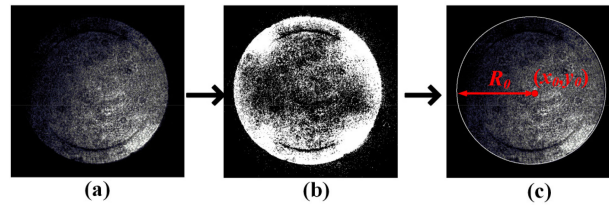


Fig. 3. (a) The cropped image; (b) The binary image of the cropped image; (c) Extracted results of the clear aperture.

### 3.1 Location of Region of Interest (ROI)

Figure 2(a) shows the originally recorded BFP image by linearly-polarized illumination. To reduce computation and remove the background noise, we locate the ROI (illumination aperture region) and crop the original BFP image. Firstly, we convert the original BFP image to a binary one to further reduce the computation and meanwhile enhance the contrast between the ROI and the background. Considering the extraordinary unevenness of the captured image due to low-quality illumination and severe coherent interference, we process the binarization using a combination of global threshold and local threshold rather than a fixed threshold. The global and local threshold values of  $v_1$  and  $v_2$  are calculated by minimum error thresholding [13], and the comprehensive threshold value  $\nu$  of each point is calculated as  $a_1 v_1 + a_2 v_2$ . The parameters  $a_1$  and  $a_2$  are adjustable according to the contrast of the aperture and the background. A relatively large block size  $w_1$  is utilized in local threshold to extract the rough profile instead of the fine details. It should be noted that, for the local threshold calculation of each pixel, the blocks are overlapped by half of the block size to avoid jumps at the block edges. Fig. 2(b) demonstrates the binarization process, in which the threshold value of the shadow region is calculated by the 4 surrounding blocks. Then the binarization value of each pixel in the coordinate  $(i, j)$  in the image is given by:

$$I_B(i, j) = \begin{cases} 0, & \text{if } I(i, j) \leq a_1 v_1 + a_2 v_2 \\ 1, & \text{otherwise} \end{cases} \quad (2)$$

where  $I(i, j)$  is the origin grayscale of each pixel. After that, the median-filtering is applied to remove the discrete noise surrounding the clear aperture (CA) on the binary image (Fig. 2(c)).

The next step is to locate the ROI on the binary image. We apply the Hough Transform (HT), a common algorithm for locating profiles in image processing, to locate the aperture profile from Fig. 2(c). The HT implementation defines a mapping from the image points into an accumulator space, which is based on the function that describes the target shape (CA profile in the paper) and achieves in a computationally efficient manner. More details on the operation of HT can be found in [14] and [15]. By HT we acquire the rough center point  $(x, y)$  and radius  $r$  of the CA (Fig. 2(d)). The original BFP image (Fig. 2(a)) is cropped to Fig. 2(e) to reduce the calculation volume and meanwhile remove the background noise. The principles of the cropping are that the CA should be at the center and there is no information loss from ROI. Here a square centered at  $(x, y)$  with an appropriate width of  $R$  is adopted. The cropped image shown in Fig. 2(e) is prepared for the following processing.

### 3.2 Center Extraction of SPs Absorption Profile

For a properly alignment system, the clear aperture and the SP absorption profile share a common center. This session is to locate the common center. Fig. 3(a) shows the cropped image from previous procedures. We firstly convert the cropped grayscale image into a binary one by using a combination of global threshold and local threshold that is  $a'_1 v_1 + a'_2 v_2$ . It should be noted that the block size of binarization  $w_2$  in this step is smaller than  $w_1$  in session 3.1 to make the ROI region in the image more uniform than the former step. The proportion of  $a'_1$  and  $a'_2$  is also adjusted to emphasize the local information. Median filtering is applied after binary process to reduce the

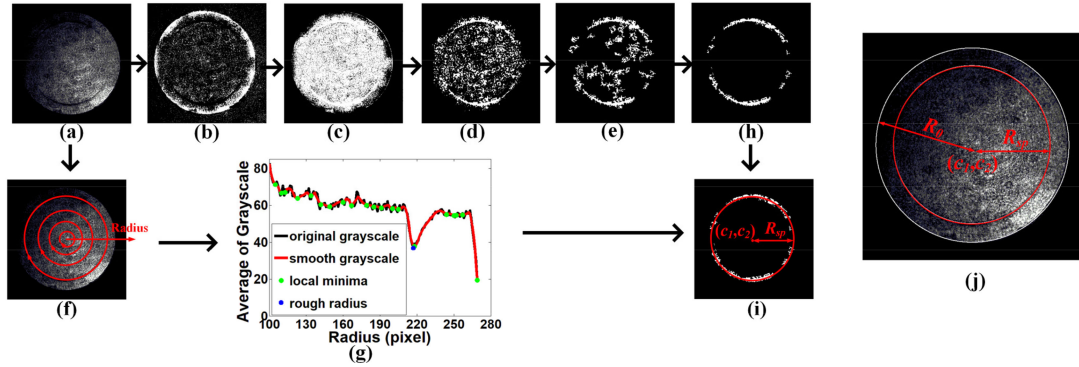


Fig. 4. (a) The cropped BFP image. (b) The binary image. (c) The reversed image. (d) The eroded image. (e) The image after wiping out pixels which have poor connectedness. (f) Statistically calculation of the grayscale along the radius. (g) Grayscale distribution along the radius. (h) Extracted coordinate of SPs profile. (i) Fitted profile of clear aperture and SPs profile on BFP. (j) Extraction result of the CA and SPs profile on BFP.

discrete noises after binarization (Fig. 3(b)). To accurately locate the center and calculate the radius, we use HT again on the homogeneous binary image which avoids the influence of the background noise and the uneven brightness after the above process. Then we get a relatively accurate radius  $R_0$  and center  $(x_0, y_0)$  through this calculation. The aperture profile is shown as Fig. 3(c).

### 3.3 SPs Profile Extraction

This section is to fit the SPs profile. Based on the cropped image shown in Fig. 4(a), firstly we choose a much smaller block size  $w_3$  compared with  $w_2$  and a much higher threshold value to emphasize the details within the aperture region, which makes the SPs profile clearly distinct from the noise. The binary image is shown in Fig. 4(b). Secondly, we reverse the binary image in Fig. 4(b) by

$$X'_{(i,j)} = 1 - X_{(i,j)} \quad (3)$$

in which  $X_{(i,j)}$  is the original intensity of the binary image and  $X'_{(i,j)}$  is the reversed intensity of each pixel. Noticing that the SPs profile is inside the aperture, we remove the background noises outside the aperture by

$$X_{(i,j)} = \begin{cases} 0, & \text{if } \sqrt{(j - x_0)^2 + (j - y_0)^2} > R_0 \\ X'_{(i,j)}, & \text{otherwise} \end{cases} \quad (4)$$

in which  $(x_0, y_0)$  and  $R_0$  are the identified aperture center and radius in Section 3.2. The processed image is shown as Fig. 4(c). Afterwards, considering that the SPs absorption profile is mostly connective, we utilize mathematical morphology [14], [15] operators such as erosion (reduction) and dilation (increase) to process the image to extract the signal and remove the noise. The erosion operation we take is expressed by:

$$X \ominus B = \{x | B_x \subset X\} \quad (5)$$

This erosion equation can be simply explained as: pixel  $x$  is removed unless each point of the structural element  $B$  translated to  $x$  is on original image  $X$ , which means that the pixels at the borders of original image and isolated points are mostly removed while the connective SPs profile remains (Fig. 4(d)). Details on mathematical morphology operations and structure elements can be found in [16] and [17]. To further eliminate noise effect of the isolated points, we calculate connectedness of

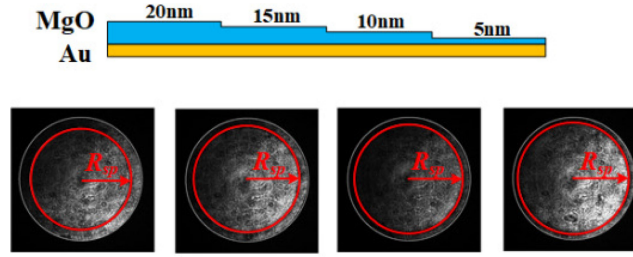


Fig. 5. Structure of the tested samples and the fitted SPs profiles when using MgO samples with thickness of 5 nm, 10 nm, 15 nm, and 20 nm MgO respectively from left to right.

each point and remove the elements which have poor connectedness. By this process, the discrete noise can be greatly reduced (Fig. 4(e)).

The next step is to locate the SPs profile. Based on the roughly identified center  $(x_0, y_0)$  of the SPs profiles in Section 3.2, we draw concentric circles with radii varying from 0 to  $r_0$  on the cropped BFP image as shown in Fig. 4(f). We statistically calculate the average intensity of the pixels on each circle and obtain the relation between the statistical intensities and the radii (Fig. 4(g)). We polyfit the curve and find the minimum which represents the roughly estimated SPs circle radius  $r_p$  as the blue star shown in Fig. 4(g). It should be noted that the last point represents the border of the aperture rather than the minimum. After this step, we remain the grayscale value of the pixels near the roughly estimated SPs region with an appropriate margin  $r_0$  and set zeros outside the region by:

$$X = \begin{cases} X_{(i,j)}, & \text{if } \sqrt{(i-x_0)^2 + (j-y_0)^2} \in (r_p - r_0, r_p + r_0) \\ 0, & \text{otherwise} \end{cases} \quad (6)$$

The term  $r_0$  is selected properly to make the coherent noise be removed to the most extent as shown in Fig. 4(h). Afterwards, we use the least square method to fit the SPs profile. The SPs profile circle is expressed as:

$$(x - c_1)^2 + (y - c_2)^2 = r^2 \quad (7)$$

where  $(c_1, c_2)$  is the center and  $r$  is the radius. We define the coordinates of the pixels in the fitted SPs profile in the above steps as  $(x_1, y_1), (x_2, y_2), \dots, (x_n, y_n)$ , and get the following over determined equations:

$$\begin{bmatrix} 2x_1 & 2y_1 & 1 \\ 2x_2 & 2y_2 & 1 \\ \dots & \dots & \dots \\ 2x_n & 2y_n & 1 \end{bmatrix} \begin{bmatrix} c_1 \\ c_2 \\ r^2 - c_1^2 - c_2^2 \end{bmatrix} = \begin{bmatrix} x_1^2 + y_1^2 \\ x_2^2 + y_2^2 \\ \dots \\ x_n^2 + y_n^2 \end{bmatrix} \quad (8)$$

By solving the equation  $Ac = d$  by  $c = (A^T A)^{-1} A^T d$ , we can get the precisely identified center  $(c_1, c_2)$  and radius  $R_{sp}$ . The fitting process of SPs profile circle is shown in Fig. 4(i). Fig. 4(j) demonstrates the precisely extracted aperture (white circle) and the SPs profile (red circle) in the original image. The results prove the efficiency of the method in identification of the plasmonic profile in BFP images with low-quality. The radii of the aperture  $R_0$  and the SPs profile circle  $R_{sp}$  are 269.65 and 214.27 pixels respectively. According to Eq. (1), the estimated plasmonic angle  $\theta_{sp}$  can be calculated to be  $44.97^\circ$ , which demonstrates an error of 1.4% compared with the theoretically calculated plasmonic angle of  $44.36^\circ$  when using the sample of 5 nm MgO layer coated on 46 nm Au layer and BK7 substrate, which corresponds to the thickness of 5.20 nm by Fresnel multilayer reflection theory [6] and shows an error of 4.0%. Similar steps are taken for other samples with different thickness as shown in Fig. 5. The MgO layers are coated on 46 nm Au layer by magnetron sputtering.  $R_{sp}$  is the fitted radius of each SPs absorption profile. The measured results are shown in Table 2. It can be

TABLE 2  
Measurement Results of Different Samples

Layer	$R_{sp}$ (pixel)	$\theta_{sp}$ (°)	MgO(nm)	Error
5nmMgO	214.27	44.97	5.20	4.0%
10nmMgO	227.84	45.44	10.46	4.6%
15nmMgO	238.73	46.61	15.24	1.6%
20nmMgO	245.22	48.40	19.65	1.75%

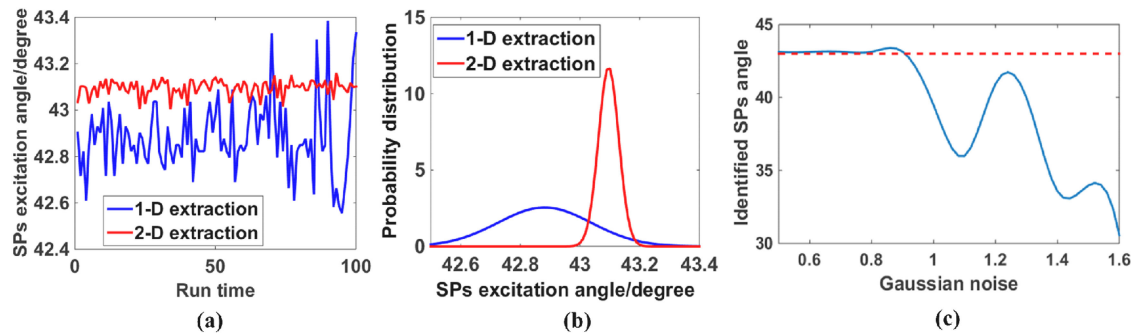


Fig. 6. (a) Identified SPs absorption profiles using 1-D line scan and the proposed 2-D identification method; (b) 1-D and 2-D identification probability distributions; (c) The relation between the identified results and Gaussian noise level.

seen that the proposed method and algorithm possesses high precision with an error blow 4.6% at 10 nmMgO, showing that the SPM allows nanoscale measurement in the axial direction.

To estimate the identification speed, we carry out the whole process and execute for 1000 loops. It takes 672 seconds in total, which means the whole algorithm process takes 672 ms on average to identify one BFP image in the test (CPU: Core i7-4770, Memory: 4G). In practice, it is unnecessary to operate the full process since outer profile of the illumination aperture and center of the SP profile is fixed. That means one just needs to identify them once for the system calibration. And only the statistically calculation is required and it takes much less time ( $\sim 98$  ms) which allows the fast identification in practice.

### 3.4 Discussion

To demonstrate the impact of coherent noises on the identification, we apply the algorithm of Monte-Carlo to compare the conventional 1-D line-scan method and the proposed 2-D morphological method. This is done by adding random noises to noise-free BFP image and repeating the process for 100 times. We statistically calculate the SPs excitation angles using the two methods. The results are shown in Fig. 6(a), which show clearly that the deviation of the 1-D identification is much larger than that of the 2-D identification and the identified results of 1-D method distribute randomly. Errors occur mostly within the SPs absorption profile where the coherent noise is severe, making average radius smaller than the SPs profile radius value. And the proposed method (red curve in Fig. 6(a)) gives relatively stable results. For clear illustration, we also give the probability distributions of the two methods as shown in Fig. 6(b). We can see that the proposed morphological method performs much better than the 1-D method with a standard deviation of 0.127 compared to 0.590, which indicates that the coherent noises are effectively reduced. Furthermore, we operate another calculation to evaluate the noise level at which the proposed method still accepts. To simulate the different levels of coherent noise, we add different variance levels of Gaussian noises to noise-free BFP image. After that we use the proposed morphological method to extract the SPs excitation

angles in these images with different noise levels. Fig. 6(c) shows the result, in which the horizontal axis indicates the variance of the added Gaussian noise. It indicates that the proposed method is applicable when the variance is as high as 0.8, which is much higher than most noise levels in experimentally obtained BFP images in practical SPMs. It is worth noting that the results are obtained by just considering the random Gaussian noise and a better evaluation can be done by using great deals of experimental data, which will be specifically investigated in the next stage.

#### 4. Conclusion

In conclusion we have proposed an automatic and high precision identification method for plasmonic absorption profile identification in objective-coupled SPM. We illustrated how the method could be applied in several typical SPMs. The details of identification procedures were given, in which we combined Hough Transform, morphology method and least-square method to extract the SPs profiles. We showed that the identification error was below 4.6% and the identification took about 98 ms for one BFP image, which promised the practical applications of SPM in fast phenomenon sensing and batches of images processing. We also discussed the impact of random coherent noises on the identification accuracy. We specifically compared the conventional 1-D line statistics and the proposed morphological method. The results showed that the proposed method could effectively eliminate the random noises and gave high accurate identified results with much smaller variance. For this reason, it could be applied in processing experimentally obtained BFP images with low quality. Note that the proposed method works well for a properly aligned SPM. The identification of SPs absorption profile for the cases of tilt sample or misaligned system is in progress.

#### References

- [1] C. L. Wong and M. Olivo, "Surface plasmon resonance imaging sensors: A review," *Plasmonics*, vol. 9, pp. 809–824, 2014.
- [2] C. E. H. Berger, R. P. H. Kooyman, and J. Greve, "Resolution in surface-plasmon microscopy," *Rev. Sci. Instrum.*, vol. 65, pp. 2829–2836, 1994.
- [3] H. Kano, S. Mizuguchi, and S. Kawata, "Excitation of surface-plasmon polaritons by a focused laser beam," *J. Opt. Soc. Amer. B*, vol. 15, pp. 1381–1386, 1998.
- [4] K. J. Moh, X. C. Yuan, J. Bu, S. W. Zhu, and B. Z. Gao, "Radial polarization induced surface plasmon virtual probe for two-photon fluorescence microscopy," *Opt. Lett.*, vol. 34, pp. 971–973, 2009.
- [5] J. Zhang, C. W. See, and M. G. Somekh, "Imaging performance of widefield solid immersion lens microscopy," *Appl. Opt.*, vol. 46, pp. 4202–4208, 2007.
- [6] H. M. Tan, "High resolution angle-scanning widefield surface plasmon resonance imaging and its application to bio-molecular interactions," Ph.D. dissertation, Univ. Nottingham, Nottingham, U. K., 2011.
- [7] H. M. Tan, S. Pechprasarn, J. Zhang, M. C. Pitter, and M. G. Somekh, "High resolution quantitative angle-scanning widefield surface plasmon microscopy," *Sci. Rep.*, vol. 6, 2016, Art. no. 20195.
- [8] B. Huang, F. Yu, and M. G. Somekh, "Surface plasmon resonance imaging using a high numerical aperture microscope objective," *Anal. Chem.*, vol. 79, pp. 2979–2983, 2007.
- [9] A. R. Halpern, J. B. Wood, Y. Wang, and R. M. Corn, "Single-nanoparticle near-infrared surface plasmon resonance microscopy for real-time measurements of DNA hybridization adsorption," *ACS Nano*, vol. 8, no. 1, pp. 1022–1030, 2014.
- [10] B. Zhang, S. Pechprasarn, J. Zhang, and M. G. Somekh, "Confocal surface plasmon microscopy with pupil function engineering," *Opt. Exp.*, vol. 20, pp. 7388–7397, 2012.
- [11] B. Zhang, C. Q. Zhang, M. G. Somekh, P. Yan, and L. Wang, "Common-path surface plasmon interferometer with radial polarization," *Opt. Lett.*, vol. 43, pp. 3245–3248, 2018.
- [12] A. W. Peterson, M. Halter, A. L. Plant, and J. T. Elliott, "Surface plasmon resonance microscopy: Achieving a quantitative optical response," *Rev. Sci. Instrum.*, vol. 87, 2016, Art. no. 093703.
- [13] J. Kittler and J. Illingworth, "Minimum error thresholding," *Pattern Recognit.*, vol. 19, pp. 41–47, 1986.
- [14] T. C. Chen and K. L. Chung, "An efficient randomized algorithm for detecting circles," *Comput. Vis. Image Understanding*, vol. 83, pp. 172–191, 2001.
- [15] M. S. Nixon and A. S. Aguado, *Feature Extraction and Image Processing*, 2nd ed. New York, NY, USA: Elsevier, 2008.
- [16] R. M. Haralick, S. R. Sternberg, and X. Zhuang, "Image analysis using mathematical morphology," *IEEE Trans. Pattern Anal. Mach. Intell.*, vol. 9, no. 4, pp. 532–550, Apr. 1987.
- [17] I. De, B. Chanda, and B. Chattopadhyay, "Enhancing effective depth-of-field by image fusion using mathematical morphology," *Image Vis. Comput.*, vol. 24, pp. 1278–1287, 2006.